Automatic Centroid Angle Measurement From CT Image for Preoperative Rod Design of Robotic-Assisted Screw–Rod System Implantation

Jiajing Zhang, *Student Member, IEEE*, Wenqing Zhang, Haodong Liu, Yingying Liu, Ningning Chen, Jianjia Zhang, and Changhong Wang

***Abstract*—Robotic-assisted implantation of screw-rod systems serves as an advanced therapy for spinal diseases. A precise curvature fit between rods and spines is critical to postoperative spinal stability. Currently, rod curvature is determined intraoperatively to accommodate screw positions, which is hardly conducive to optimal rod bending and is vulnerable to surgeons' expertise. To address this challenge, we propose an automated and efficient method for measuring the centroid angle to guide preoperative rod design from CT images. The centroid angle is defined by lines connecting centroids of the upper and lower vertebrae pairs, providing a reliable measurement for spinal deformities. The proposed pipeline includes (1) 3D spine segmentation with multiscale multitask deep learning; (2) vertebrae recognition using graphical morphology; (3) automatic and reproducible centroid angle measurement. Our method is evaluated on both healthy and pathological spines. Compared to manual measurements by professional surgeons, our method achieves an accuracy of 94.50% and 91.93% on adjacent and non-adjacent vertebrae, respectively. A Slicer-based plugin for robotic-assisted screw-rod systems implantation is built, providing a new clinical tool to personalize screw-rod systems consistent with the natural spinal curvature, thereby enhancing biomechanical properties.**

***Index Terms*—Image-guided treatment, screw-rod system, spine, surgical robot, centroid angle, preoperative CT image.**

I. Introduction

SPINAL disorders, including low back pain, spinal cord injury, and scoliosis, are prevalent diseases around the world. Specifically, low back pain and spinal cord injury affect 619 million [1] and 9 million [2] patients worldwide, respectively; primary degenerative scoliosis holds a global prevalence of 37.6% among adults [3]. These spinal disorders impede the function and stability of the spine and have become one of the leading causes of disability worldwide [4]. A common therapeutic approach for these diseases is screw-rod systems, known for their excellent biomechanical properties in spinal fixation [5], [6], [7]. A screw-rod system comprises multiple pedicle screws and a rod on each side; the screws are inserted into the vertebrae, and the rod is affixed to these screws. Currently, the implantation of screw-rod systems requires surgeons to manually bend the rods intraoperatively to align with the implanted screws, a process that heavily relies on the surgeon's experience and skill.

Since the introduction of the first spinal surgical robot, SpineAssist (Mazor Robotics Ltd., Caesarea, Israel), from 2004 [8], robotic-assisted screw implantation systems have progressed considerably [9], [10], [11]. The rapid evolution of computer-aided technologies in this field has profoundly enhanced surgical navigation [12] and facilitated the adoption of minimally invasive surgical techniques [13]. Current protocols for robot-assisted screw-rod systems typically commence with the identification of the affected vertebral segment, followed by the programming of insertion paths, and the placement of screws. Subsequently, the rods are manually bent to conform to the screw alignments. However, most existing systems overlook the critical influence of the rod structure [14]. They often neglect to ensure proper fitting of rods and the spine, which is vital for successful therapy.

For experienced surgeons, manual rod bending is typically not a challenge, as years of practice and expertise enable them to efficiently bend high-quality rods. In contrast, novice surgeons may produce suboptimal rod shapes during intraoperative bending, resulting in compromised biomechanical outcomes [15]. This can lead to complications such as rod breakage, screw loosening, adjacent segment disease, and prolonged recovery times. Therefore, an automated tool providing spinal curvature measurement and accurate rod bending guidelines can be beneficial for training or reassuring novice surgeons.

While current robotic systems mainly focus on screw insertion, offering less blood loss and lower reoperation rate [16], they lack a robust mechanism for the preoperative design and

Received 28 April 2024; revised 28 June 2024 and 18 July 2024; accepted 15 August 2024. Date of publication 19 September 2024; date of current version 12 November 2024. This article was recommended for publication by Associate Editor G. Dagnino and Editor P. Dario upon evaluation of the reviewers' comments. This work was supported in part by Covidien (China) Medical Devices Technology Company Ltd., in part by the National Natural Science Foundation of China under Grant 62303496, Grant 62471501, Grant 62101611, and in part by the Guangdong Basic and Applied Basic Research Foundation under Grant 2021A1515110029, and Grant 20212023A1515012278). *(Corresponding author: Changhong Wang.)*

Jiajing Zhang was with the School of Biomedical Engineering, Shenzhen Campus of Sun Yat-sen University, Shenzhen 518107, China. He is now with the Department of Electrical and Electronic Engineering, The University of Hong Kong, Hong Kong (e-mail: jiajingz@connect.hku.hk).

Wenqing Zhang, Haodong Liu, Jianjia Zhang, and Changhong Wang are with the School of Biomedical Engineering, Shenzhen Campus of Sun Yat-sen University, Shenzhen 518107, China (e-mail: qingh1008@gmail.com; liuhd26@mail2.sysu.edu.cn; zhangjj225@mail.sysu.edu.cn; wangchh55@mail.sysu.edu.cn).

Yingying Liu was with Covidien (China) Medical Devices Technology Company Ltd., Shanghai 201114, China (e-mail: lyy0226@outlook.com).

Ningning Chen is with the Department of Orthopedic Surgery, The Seventh Affiliated Hospital, Sun Yat-sen University, Shenzhen 518107, China (e-mail: chennn8@mail.sysu.edu.cn).

Digital Object Identifier 10.1109/TMRB.2024.3464106

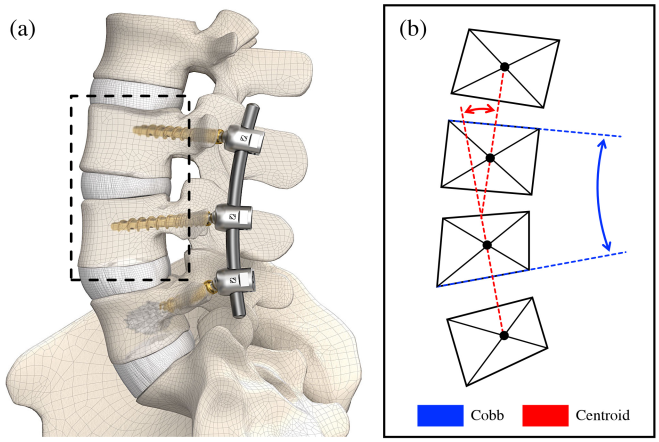

Fig. 1. Diagram of anatomy geometry: (a) A screw-rod system implanted in a spine (Diplomat system, Signus, Germany); (b) Definitions of the Cobb angle and the centroid angle, calculated on vertebrae in black dashed box.

prefabrication of rods. Since each patient's spinal curvature is unique, developing algorithms that can accurately model these variations and translate them into precise rod curvatures is still challenging. Preoperative design and prefabrication of rods could ensure that rod curvature matches the physiological spinal curvature, thereby optimizing the mechanical properties of the implant and minimizing human errors associated with inexperience and variability. Therefore, this could benefit patient care in spinal surgery and make novice surgeons more confident in rod placement.

Studies have established a significant correlation between the curvature of the screw-rod system and postoperative spinal stability [17]. The rod primarily dictates the curvature of this system. When the curvature of the rods does not align with that of the implanted spine, complications such as adjacent segment disease, postoperative back pain, or even spinal degeneration may arise [15]. Therefore, it is crucial to consider the spinal curvature characteristics for the robotic-assisted implantation of screw-rod systems. In modern spinal disease therapy, there exists a pressing need for an accurate and efficient preoperative rod design method that can adapt to the natural curvature of the spine. This advancement is essential for enhancing the development of robot-assisted screw-rod systems in a more intelligent, scientifically grounded, and personalized manner.

The Centroid Angle (CA) is commonly employed in clinical practice for measuring conditions such as scoliosis [18] and lordosis [19]. As depicted in Fig. 1 (b), it is defined by lines passing through the centroids of two upper and two lower vertebrae [20]. In comparison to other metrics such as the Cobb angle and tangent angle, which heavily rely on the quality of vertebral endplates, the CA remains relatively stable across a broad spectrum of spinal lesions and imaging conditions [21]. This stability arises because the position of the vertebral centroid is less affected by endplate tilting, vertebral injury, or manual intervention than vertebral edges [18]. Nevertheless, the current clinical approach requires physicians to manually measure CA, which is time-consuming and labor-intensive. Manual measurement demands substantial expertise and produces results that are challenging to reproduce. Moreover, existing research on CA primarily focuses on assessing scoliosis and lordosis [18], rather than optimizing rod structure in screw-rod systems. Hence, an automatic CA measuring approach via CT images for preoperative rod design has shown substantial clinical necessity.

To this end, we integrate deep learning and morphological computation algorithms to automatically compute sagittal CA from preoperative CT images. Subsequently, we utilize this measurement to guide rod design by aligning its curvature with that of the implanted spine. Finally, we develop a practical and automatic plugin based on Slicer for clinical application. The primary contributions of this study are as follows:

- *Spine-aware VNet with adaptive sampling mode:* We propose a spine segmentation model for preoperative CT images, featuring a threshold-based sampling mode and multi-task learning strategy with multi-scale spine awareness. This approach aims to reduce impurities in segmentation maps and enhance the precision of spine boundary delineation.
- *Vertebrae recognition in the sagittal plane:* We propose a vertebrae recognition method based on image attribute clustering and corner point detection. The integration of the two branches achieves high precision and specificity in vertebral recognition, thereby avoiding misdetections and omissions.
- *Automatic CA measurement:* We extract vertebral centroids to automate CA measurement. Compared with manual measurement, it facilitates an objective and reproducible quantification of spinal curvature across any vertebral section.
- *Preoperative rod design:* We integrate the above techniques to develop a preoperative rod design plugin using 3D Slicer. Specifically, we focus on enhancing operational efficiency by implementing user-friendly clinical interactions.

II. Method

The proposed pipeline for CA measurement consists of three main stages, respectively named *Spine Segmentation on CT Image* (Section II-A), *Vertebrae Recognition in Sagittal Plane* (Section II-B), and *Automated Centroid Angle Measurement* (Section II-C). To boost clinical transformation, we integrate the above stages to develop a *Slicer-based plugin for preoperative rod design* (Section II-D).

A. Spine Segmentation on CT Image

Fast and high-precision 3D spine segmentation is vital for both CA measurements and rod design. For accelerating segmentation, we propose an adaptive threshold-based sampling mode for data loading without any preprocessing. To further improve segmentation quality, we develop Spine-aware VNet, a multi-scale, multi-task learning 3D segmentation model.

1) Adaptive Threshold-Based Sampling Mode: The spine CT image is voluminous, as illustrated in Fig. 2 (a). A sub-sampling strategy is needed to divide an entire CT volume into multiple small 3D patches: $\mathfrak{I} \in \mathbb{R}^{L\times W\times H} \mapsto$

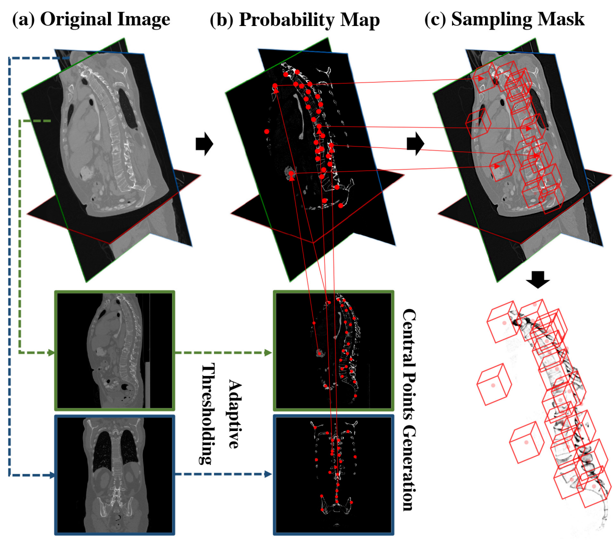

Fig. 2. Diagram of our adaptive threshold-based sampling mode: (a) The original volumetric CT image; (b) The probability map to generate sampling centers; (c) The sampling mask located at central points, covering full spine regions.

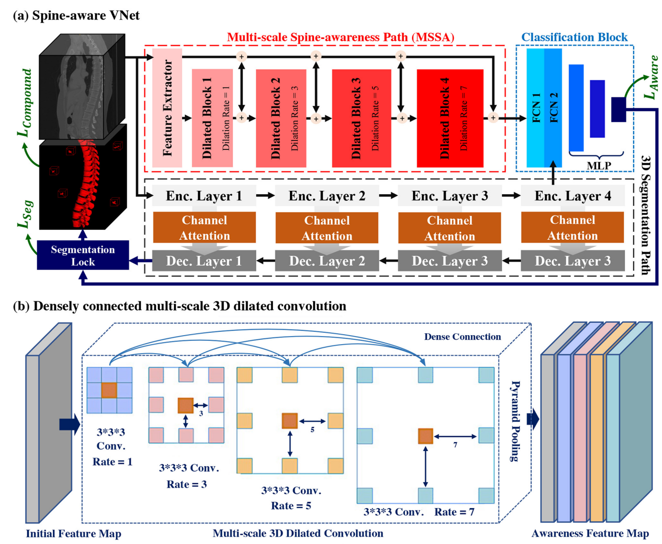

Fig. 3. (a) Spine-aware VNet: The red dashed box shows the multi-scale spine-awareness path; The black dashed box shows the segmentation path; The blue dashed box shows the classification block. (b) Densely connected multi-scale 3D dilated convolution in MSSA with four dilated rates.

$\{I_1^{(x_1,y_1,z_1)}, \ldots, I_n^{(x_n,y_n,z_n)}\} \in \mathbb{R}^{n\times k\times k\times k}$, where $\mathfrak{I}$ denotes a full CT image before sampling, I_n denotes a sampled 3D patch centered at (x_n, y_n, z_n), n denotes the number of patches, k denotes the length of each cube patch.

Uniform sampling is the most common solution but often leads to an overabundance of sampled patches that encompass unnecessary regions, imposing a significant computational burden in clinical scenarios. It also exacerbates class imbalance between spinal and non-spinal regions, thereby complicating training efforts. Therefore, a mode with adaptive selection of sampling points is needed. Adaptive sampling refers to an algorithm that approximately locates the spine in each CT volume and assigns most of the sampling points to it, reducing oversampling.

To this end, we propose a 3D sampling mode based on adaptive thresholding. Leveraging the characteristic high Hounsfield Unit (Hu) values of spinal bones in CT images, typically exceeding 1000 Hu, our mode generates a sampling probability map $\tilde{\Psi}$ for each CT image by Otsu thresholding [22]: $\tilde{\Psi} = f_{\text{Ostu}}(\mathfrak{I}) \in \mathbb{R}^{L\times W\times H}$. Let $p^{(x_i,y_i,z_i)}$ denote the pixel value of point (x_i, y_i, z_i), T denote the Ostu thresholding, N_1 and N_2 be the total number of pixels in the foreground and background, μ_1 and μ_2 be their average grey values, respectively. The Ostu thresholding can be represented as

$$f_{\text{Ostu}}(\mathfrak{I}) : p^{(x_i,y_i,z_i)} \geq arg \max_{\text{T}} \left[\frac{N_1}{N} \cdot \frac{N_2}{N} \cdot (\mu_1 - \mu_2)^2\right] \quad (1)$$

for $i = 1, \ldots, L \times W \times H$. As shown in Fig. 2 (b), skeletal regions appear at a high sampling rate in $\tilde{\Psi}$. And we randomly select n points in $\tilde{\Psi}$ as central points to locate the final sampling masks in Fig. 2 (c): $\tilde{\Psi} \mapsto \Psi$. Given that the spine typically represents the largest skeletal structure in thoracic and abdominal CT images $\mathfrak{I}$, our central points are concentrated around the spine and its vicinity. The i-th sampling patch is defined as a cube $I^{(x_i,y_i,z_i)} \in \mathbb{R}^{k\times k\times k}$, where $(x_i, y_i, z_i) \in \Psi$. Finally, we reconstruct a complete 3D spine by assembling the segmentation maps of each patch.

2) Spine-Aware VNet: Spine-aware VNet equips V-Net [23] with spine-awareness via multi-task learning, enabling it to detect spine regions across multiple scales. This model performs 3D spine segmentation while concurrently assessing whether each patch contains spinal regions, thereby optimizing the segmentation map accordingly. The structure of Spine-aware VNet, illustrated in Fig. 3(a), comprises three components: a 3D segmentation path, a multi-scale spine-awareness path, and a classification block.

In the 3D segmentation path, we develop a Vnet-like backbone, comprising an encoder and a decoder, interconnected by skip connections. Specifically, the encoder consists of four 3D convolutional layers $f_c : X_l^c \mapsto \lambda_l^{2c}$. Each layer performs two sequential 3D convolutions using a kernel $\mathcal{W} \in \mathbb{R}^{5\times 5\times 5}$, with a bias b, and a stride of 1. These convolutions are followed by batch normalization and ReLU activation functions. The output λ of the t-th convolution in the l-th layer is represented as

$$\lambda_{l,t}^c = f_{\text{ReLU}}\big(f_{\text{BN}}\big(\mathcal{W}_{l,t}^T \lambda_{l,t-1}^c + b_{l,t}\big)\big), l \in [1, 4], t \in [1, 2] \quad (2)$$

Then we add the inputs of this layer to the feature map via residual connection: $\lambda_{l,r}^c = X_l^c + \lambda_{l,2}^c$. Finally, we perform a refine convolution $f_{\text{rfc}} : \lambda_{l,2}^c \mapsto \lambda_{l,3}^{2c}$, with a kernel of $\mathcal{W} \in \mathbb{R}^{2\times 2\times 2}$ and a doubled output channel. The initial output channel of the first layer is set to 16. The decoder also consists of four 3D deconvolution layers denoted as f_{dc}. Unlike the encoder, each layer in the decoder utilizes transposed convolution and takes input from the corresponding layers of encoder and decoder. Therefore, the l-th layer is represented as $\bar{\lambda}_l = f_{\text{dc}}[f_{\text{cha}}(\lambda_{l-1}) \oplus \bar{\lambda}_{l-1}]$, where $\oplus$ denotes a concatenation and f_{cha} denotes channel attention mentioned below.

Due to the stochastic distribution of sampling centers, the sampling process inherently results in varying proportions of spine inclusion, categorized into four types: 1) patches with

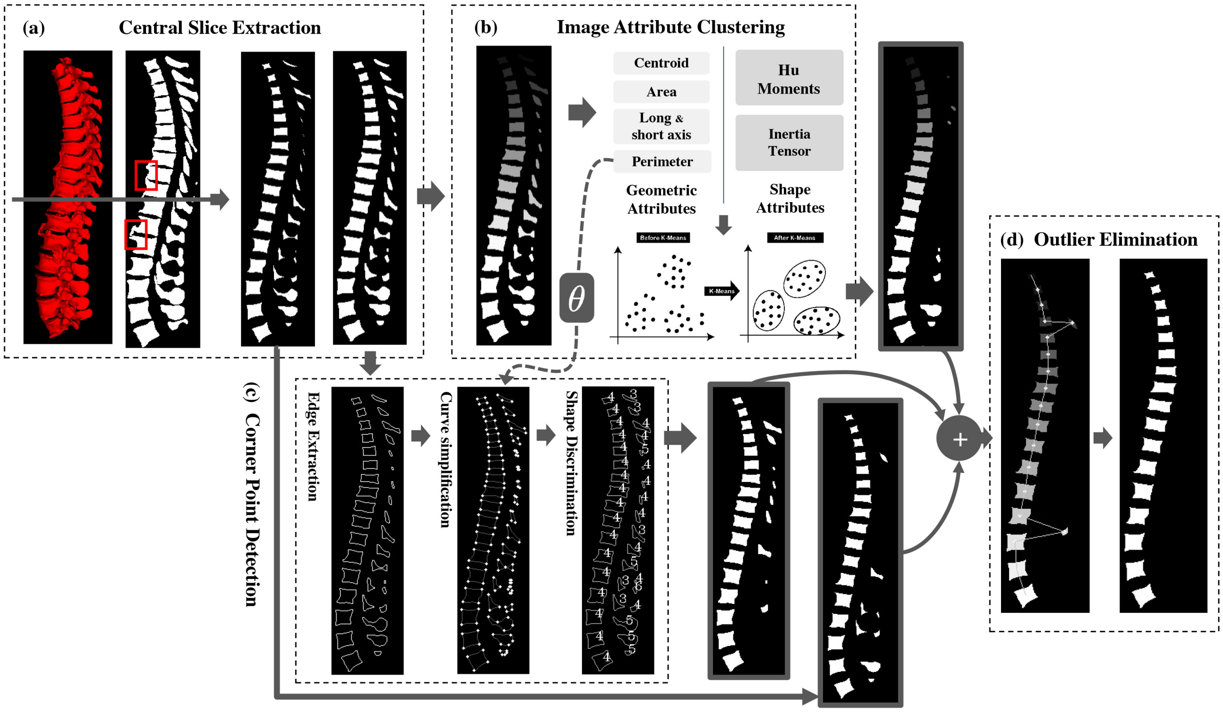

Fig. 4. The workflow of our vertebrae recognition in the sagittal plane: (a) Central slice extraction with a subsectional strategy; (b) Vertebrae recognition branch based on IAC; (c) Vertebrae recognition branch based on CPD; (d) Outlier elimination based on vertebral linkage angle.

at least one intact vertebra, 2) patches with large incomplete vertebra, 3) patches with fragmented vertebras, and 4) patches without vertebra. To address this variability, we develop a multi-scale spine awareness (MSSA) path to capture size-stable vertebral features. Firstly, MSSA takes a patch as input and initializes the image features by a feature extractor including four convolutional layers.

Inspired by the Atrous Spatial Pyramid Pooling (ASPP) [24], MSSA cascades four 3D dilated blocks with dilation rates of 1, 3, 5, and 7 to extract multi-scale spine features from local to global contexts (as shown in Fig. 3(b)), corresponding to the four types of patches: $M_{\text{dilate}} = \{\mathcal{D}_{1,1}, \mathcal{D}_{2,3}, \mathcal{D}_{3,5}, \mathcal{D}_{4,7}\}$. Each 3D dilated block begins with an initial convolution with $\mathcal{W}_{l,1} \in \mathbb{R}^{1\times1\times1}$, getting initial feature $\lambda_{l,1} \in \mathbb{R}^{l\times w\times h}$. Then a dilated convolution is performed, which inserts cavities into convolution kernels $\mathcal{W}_{l,2} \in \mathbb{R}^{3\times3\times3}$, enlarging its receptive fields without increasing parameters. By setting different dilation rates d, MSSA captures semantic features in different receptive fields:

$$\mathcal{D}_{l,d}^{(i,j,k)} = \sum_{p=-1}^{1}\sum_{m=-1}^{1}\sum_{n=-1}^{1} \left(\lambda_{l,1}^{(i+p\cdot d,\ j+m\cdot d,\ k+n\cdot d)} \cdot \mathcal{W}_{l}^{(p,m,n)} + b_l\right) \tag{3}$$

where $\mathcal{D}_{l,d}^{(i,j,k)}$ represents the output of the l-th block at spatial position (i, j, k) with a dilation rates d. In addition, MSSA adopts pyramid pooling [25], $f_{\text{PP}} : \mathcal{D}_{l,d} \in \mathbb{R}^{c,*,*,*} \mapsto \mathcal{D}_{l,d} \in \mathbb{R}^{c,l,w,h}$, where * denotes various feature sizes of difference layers. It pools feature maps at different scales to a fixed size, maintaining dimensional stability while yielding a richer feature representation. Finally, MSSA concatenates four multi-scale feature maps together as its output M_{dilate}.

The multi-task learning of Spine-aware VNet comprises the MSSA, the encoder, a classification block, and a segmentation lock. The classification block takes the output of MSSA (M_{dilate}) and the output of the 4-th layer encoder (λ_{enc}) as input. It performs fully connected operations on these inputs separately, then concatenates and feeds them into a multilayer perception machine (MLP). The MLP has three layers with 64, 32, and 1 neurons, respectively. Then we get a binary indicator $\mathcal{C}$ after a sigmoid activation. The classification block here discriminates whether the current patch contains a spine region.

The segmentation lock determines the effectiveness of the decoder output ($\bar{\lambda}_{\text{dec}}$) based on the classification result ($\mathcal{C}$). If $\mathcal{C} = 0$, the corresponding patch is excluded from both training and 3D spine reconstruction. The segmentation map is set to blank, thereby invalidating segmentation training for that patch. Nonetheless, the classification block is still updated according to the classification results. Conversely, if $\mathcal{C} = 1$, the patch is considered effective and is included in backpropagation and 3D reconstruction. Ultimately, the segmentation lock reconstructs the final 3D spine model $\mathfrak{S}$ using all validated segmentation results. Moreover, because the two tasks share the encoder of the segmentation path, the overwhelmed classification task may impose a negative interference on the segmentation task. Therefore, we insert channel attention (f_{cha}) into skip connections to enhance synergistic features and suppress interfering features, where only beneficial features from the encoder can be introduced into the decoder.

In terms of loss function, besides segmentation loss (Eq. (4)), we introduce compound loss (Eq. (5)) and awareness loss (Eq. (6)). Segmentation loss and compound loss respectively measure the consistency of the original segmentation

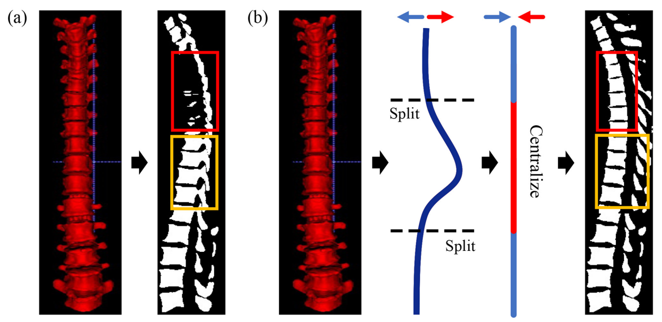

Fig. 5. (a) Sagittal central slices extraction without subsectional strategy; (b) sagittal central slices extraction with subsectional strategy.

map ($y_{\mathrm{Seg}} = \bar{\lambda}_{\mathrm{dec}}$) and the compound segmentation map ($y_{\mathrm{Comp}} = \mathfrak{S}$) with the labels ($\hat{y}$). They include pixel-level weighted binary cross-entropy loss and Dice loss. The awareness loss, a binary cross-entropy loss, measures the consistency of the classification results ($\gamma = \mathcal{C}$) with the true situation ($\hat{\gamma}$). Since the segmentation task is the actual target in our study, we apply a weighted joint loss function as Eq. (7):

$$L_{\mathrm{Seg}} = L_{\mathrm{WBCE}}\big(y_{\mathrm{Seg}},\ \hat{y}\big) + L_{\mathrm{Dice}}\big(y_{\mathrm{Seg}},\ \hat{y}\big) \tag{4}$$

$$L_{\mathrm{Comp}} = L_{\mathrm{WBCE}}\big(y_{\mathrm{Comp}},\ \hat{y}\big) + L_{\mathrm{Dice}}\big(y_{\mathrm{Comp}},\ \hat{y}\big) \tag{5}$$

$$L_{\mathrm{Aware}} = -\frac{1}{\eta}\sum_{i=1}^{\eta}\big(\gamma_i \log \hat{\gamma}_i + (1-\gamma_i)\log(1-\hat{\gamma}_i)\big) \tag{6}$$

$$L = W_{\mathrm{aware}}\ L_{\mathrm{Aware}} + W_{\mathrm{Seg}}\ L_{\mathrm{Seg}} + W_{\mathrm{Comp}}\ L_{\mathrm{Comp}} \tag{7}$$

B. Vertebrae Recognition in Sagittal Plane

In sagittal CT slices, both vertebral bodies and vertebral arches are visible. Since CA only pertains to the centroidal characteristics of vertebral bodies, it is crucial to exclude the interference of vertebral arches. To achieve this, we propose a method to recognize vertebral bodies in the sagittal plane, as shown in Fig. 4. Firstly, this method inherits the 3D spine model produced by the Spine-aware VNet. A subsectional strategy is designed to extract the spinal central slice. Subsequently, we introduce two vertebrae recognition branches: one based on image attribute clustering (IAC) and the other on corner point detection (CPD). Finally, a voting scheme combines results from both branches and performs outlier elimination according to vertebral linkage angles to further improve recognition accuracy.

1) Central Slice Extraction: Most spine diseases affect spinal morphology, where the most common abnormality is a deviation of the spinal axis. In an original central slice, this deviation could lead to missing vertebrae as the red box in Fig. 5(a) and adhesions between vertebrae and arch as the yellow box. Hence, our method carries a subsectional strategy based on the anatomical divisions of the spine. The whole spine model is divided into cervical, thoracic, and lumbar subsections. This strategy leverages the inherent distinct curvature of these three subsections. Specifically, the cervical subsection corresponds to the upper spine, including the neck vertebrae (C1-C7); the thoracic subsection covers the middle spine, encompassing the thoracic vertebrae (T1-T12); and the lumbar subsection pertains to the lower spine, including the lumbar vertebrae (L1-L5). Then we extract three central slices separately and centralize them to get a final central slice ($\mathfrak{C}$). To further remove adhesions between adjacent vertebrates, we apply erosion and dilatation to get $\mathfrak{C}_{\mathrm{ers}}$ and $\mathfrak{C}_{\mathrm{dia}}$.

2) Image Attribute Clustering Branch: Fig. 4(b) shows our image attribute clustering branch for vertebrae recognition. Initially, it employs an eight-neighborhood connected component algorithm [26] to label each individual region on $\mathfrak{C}_{\mathrm{dia}}$. Subsequently, it evaluates five geometric attributes and two shape attributes for each region. The geometric attributes include centroidal coordinates, long axis, short axis, area, and perimeter. In terms of shape, vertebrae tend to be regular rectangles. In contrast, arches appear variously. To quantify the discrepancy between both shapes, Hu moment and inertia tensor are applied. Hu moments combine and normalize geometric moments to describe pixel distribution in the spatial domain, providing shape representation with rotation, translation, and scaling invariance [27]. Additionally, the inertia tensor, a second-order tensor incorporating pixel spatial locations and values, extracts key shape features of edge orientation, angle, and curvature.

We normalize the seven attributes and then classify all regions into two classes by K-means clustering. The class with a larger total area is retained in the output Υ_{IAC} as the vertebrae class.

3) Corner Point Detection Branch: Another vertebrae recognition branch employs a corner point detection methodology. In the sagittal plane, vertebrae typically exhibit a rectangular cross-section characterized by four corner points. Therefore we detect the number of corner points $\mathcal{N}_i$ on each connected component, as shown in Fig. 4 (c).

Firstly, we apply the Canny operator [28] to extract the edges, transforming image regions into curves. Using Douglas-Peucker algorithm [29], we fit each edge $E_i = \{p_0, p_1, \ldots, p_m\}$ to a polyline that retains the essential shape with fewer points by curve simplification. As shown in Eq. (8), we set a threshold θ and calculate the maximal distance $d_{\perp}(p_k)$ from any point p_k to the line linking the start point p_0 to the endpoint P_m. If $d_{\perp}(p_k) > \theta$, p_k is marked as a new key point. Otherwise, all points between p_0 and p_m are discarded, retaining only p_0 and p_m as key points. This process is then iteratively applied to the new subsets $p_0, p_1, \ldots, p_k$ and $p_k, p_{k+1}, \ldots, p_m$ until all key points are marked.

$$f_{\mathrm{dp}}(E_i, \theta) = \begin{cases} \{p_0, p_m\} \cup f_{\mathrm{dp}}(P_{0k}, \theta) \cup f_{\mathrm{dp}}(P_{km}, \theta) & , d_{\perp}(p_k) > \theta \\ \{p_0, p_m\} & , \text{otherwise} \end{cases} \tag{8}$$

where the parameter $\theta_i = 0.05 \times l(E_i)$ is dependent on the perimeter $l(E_i)$ of each edge E_i to adapt to diverse area sizes. We then count the number of corner points $\mathcal{N}_i$. When $\mathcal{N}_i = 4$, rectangular components are retained as vertebra; when $\mathcal{N}_i \neq 4$, irregular components are excluded.

Shape features are altered following erosion and dilation operations, each contributing uniquely to our CPD method. Therefore, we design separate erosion and dilation branches. Finally, we derive the outcome by intersecting the results from both branches: $\Upsilon_{\mathrm{CPD}} = f_{\mathrm{dp}}(\mathfrak{C}_{\mathrm{ers}}) \cap f_{\mathrm{dp}}(\mathfrak{C}_{\mathrm{dia}})$.

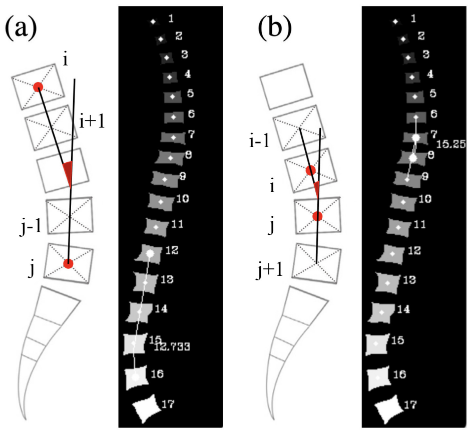

Fig. 6. Two situations of CA measurement: (a) Non-adjacent measurement, (b) Adjacent measurement.

4) Outlier Elimination Based on Vertebral Linkage Angle: Voting the vertebrae recognition results from the above subsection (2) and (3) yields an initial vertebrae map: $\Upsilon_{\text{init}} = \Upsilon_{\text{IAC}} \cap \Upsilon_{\text{CPD}}$. As illustrated in Fig. 4 (d), we further refine the recognition according to prior knowledge that linkage angles of adjacent vertebrae along the spine axis are obtuse. We take the centroid ϑ_i of each region on Υ_{init} and link the neighboring centroids to form the linkage angle δ_i:

$$\delta_i = \arccos\left(\frac{\overrightarrow{\vartheta_{i+1}\vartheta_i} \cdot \overrightarrow{\vartheta_i\vartheta_{i-1}}}{\left\|\overrightarrow{\vartheta_{i+1}\vartheta_i}\right\| \cdot \left\|\overrightarrow{\vartheta_i\vartheta_{i-1}}\right\|}\right), \tag{9}$$

where $i = 2 \sim n-1$. If $\delta_i < \frac{\pi}{4}$, the region where ϑ_i belongs is distant from the spine axis. Thus it can be defined as an outlier that is highly probable to be an arch or other non-vertebral region. As a result, we eliminate all outliers and output purified vertebrae map Υ_{out}.

C. Automated Centroid Angle Measurement

According to the clinical definition [20], we develop an algorithm to automate CA measurement. This algorithm inherits the centroid set $\{\vartheta_1, \ldots, \vartheta_n\}$ derived from sagittal vertebrae recognition Section II-B, and accepts the vertebral section $[v_i, v_j]$ to be measured as user input. In clinical practice, CA measurement encompasses two scenarios:

1) Non-Adjacent Measurements: As shown in Fig. 6(a), non-adjacent measurement $\dot{\Lambda}i, j$ represents a non-adjacent measurement is defined by vector $\overrightarrow{\vartheta i\vartheta_{i+1}}$ and vector $\overrightarrow{\vartheta_j\vartheta_{j-1}}$. $\overrightarrow{\vartheta_i\vartheta_{i+1}}$ links the centroids of the upper vertebra v_i and its adjacent lower vertebra v_{i+1}, while $\overrightarrow{\vartheta_j\vartheta_{j-1}}$ connects the centroids of the lower vertebra v_j and its adjacent upper vertebra v_{j-1}:

$$\dot{\Lambda}_{i,j} = \arccos\left(\frac{\overrightarrow{\vartheta_i\vartheta_{i+1}} \cdot \overrightarrow{\vartheta_j\vartheta_{j-1}}}{\left\|\overrightarrow{\vartheta_i\vartheta_{i+1}}\right\| \cdot \left\|\overrightarrow{\vartheta_j\vartheta_{j-1}}\right\|}\right). \tag{10}$$

2) Adjacent Measurements: As shown in Fig. 6(b), adjacent measurement $\ddot{\Lambda}i, j$ is defined by vector $\overrightarrow{\vartheta i\vartheta_{i-1}}$ and vector $\overrightarrow{\vartheta_j\vartheta_{j+1}}$. $\overrightarrow{\vartheta_i\vartheta_{i-1}}$ links the centroids of the upper vertebra v_i and its adjacent upper vertebra v_{i-1}, while $\overrightarrow{\vartheta_j\vartheta_{j+1}}$ connects the centroids of the lower vertebra v_j and its adjacent lower vertebra v_{j+1}:

$$\ddot{\Lambda}_{i,j} = \arccos\left(\frac{\overrightarrow{\vartheta_i\vartheta_{i-1}} \cdot \overrightarrow{\vartheta_j\vartheta_{j+1}}}{\left\|\overrightarrow{\vartheta_i\vartheta_{i-1}}\right\| \cdot \left\|\overrightarrow{\vartheta_j\vartheta_{j+1}}\right\|}\right). \tag{11}$$

Finally, we output centroid angle $\dot{\Lambda}_{i,j}$ or $\ddot{\Lambda}_{i,j}$ as the curvature of vertebra section $[v_i, v_j]$.

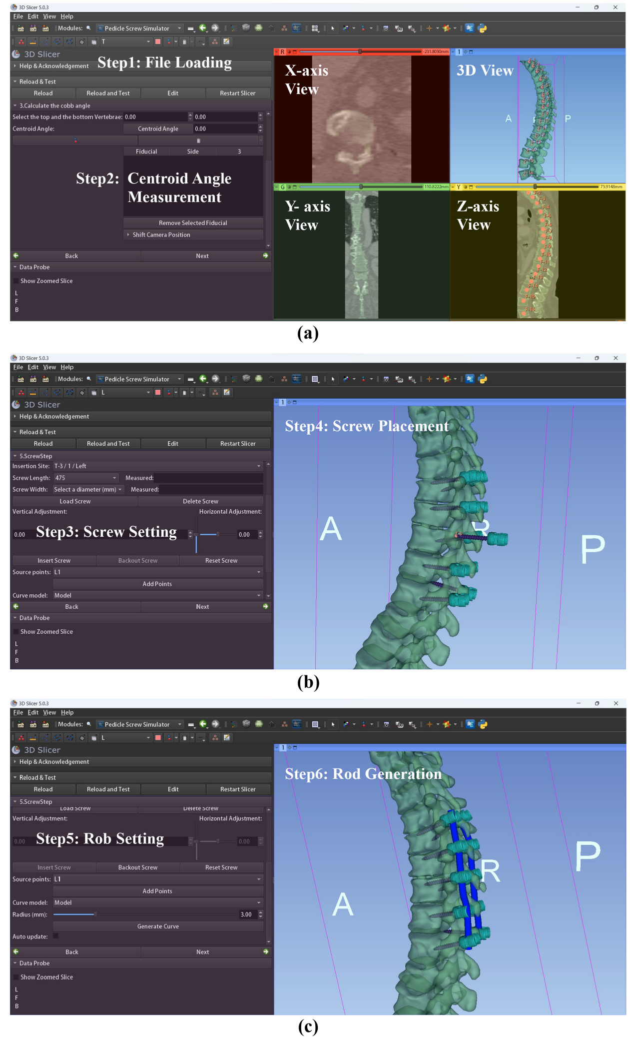

Fig. 7. The screenshot of (a) file system and display, (b) screw placement, and (c) rod generation in our application.

D. Slicer-Based Application

We develop a Slicer-based plugin to implement a clinically accessible preoperative rod design for screw-rod systems. Besides spine segmentation, vertebrae recognition, and CA calculation above, this plugin also integrates file system and display (Fig. 7.a), screw placement (Fig. 7.b), and rod generation (Fig. 7.c) functions.

1) File System and Display: Our plugin seamlessly loads CT files in DICOM or nii formats, eliminating the need for preprocessing. It automatically initiates 3D spine segmentation upon loading and performs sagittal vertebra recognition in the background. The plugin then displays slice views in three orthogonal axes and presents a comprehensive 3D visualization of the spine model. Furthermore, it integrates the results of sagittal vertebrae recognition into the 3D spine model, annotating vertebrae numbers for enhanced spatial orientation.

2) Screw Placement: Our plugin requires the user to specify the vertebral section targeted for screw-rod system implantation. Initially, each screw should be placed into the designated pedicle, guided by clinical anatomical landmarks to determine the insertion location and angle. Surgeons can adjust the screw in the 3D space based on their clinical experience. Additionally, the plugin permits customization of screw length, diameter, and insertion depth to accommodate individual anatomical differences.

3) Rod Generation: In typical screw-rod systems, two rods are aligned with screw columns on each side of the spine. Based on clinical research [30], a rod curvature that ranges between plus or minus 4∼8 degrees relative to centroid angle is recommended, to ensure the rods fit the spinal curvature properly. Therefore, Our plugin generates a rod with a curvature equal to the centroid angle initially. Then control points from screw cap positions are set for manual adjustment. New control points can be added along the rob by surgeons if necessary, which will be connected via cardinal B-splines to form the updated curved shape. While screw or control points adjustment, the plugin actively monitors the revised rod curvature, providing alerts if adjustments compromise spinal alignment. This dynamic feedback ensures that each rod's final curvature is anatomically constrained, enhancing surgical outcomes by maintaining biomechanical integrity.

Clinically, our Slicer plugin can be easily integrated into existing surgical paradigms for robot-assisted implantation of screw-rob systems, where the plugin mainly contributes to preoperative planning and surgical navigation. Specifically, the anticipated steps are as follows: (i) Load a patient's preoperative CT images, and the plugin automatically reconstructs an accurate 3D spine model for surgical planning; (ii) Select the vertebral segment to be implanted and insert the screws, then the plugin automatically calculates the spinal curvature to generate the optimal rod shape; (iii) Adjust, if necessary, the recommended screw-rob system displayed on the 3D space; (iv) Fabricate the pre-designed rod preoperatively by rod bending machine [31], rather than manually bending it intraoperatively; (v) Use an available robotic-assisted surgical system to insert screws according to our planned screw location and implant our pre-designed rods. Since no manual operation, such as bending the rods and locating the screws, is required intraoperatively, this plugin makes it feasible to perform a fully robotic-assisted implantation, driving it toward a more intelligent and automated scenario.

III. Experiment and Result

A. Spine Segmentation on CT Image

1) Implementation Details: To validate the advanced performance of our adaptive threshold-based sampling mode and Spine-aware VNet for CT spine segmentation, a series of experiments are conducted. The Spine-aware VNet is built on Python 3.8 (Python Software Foundation, PSF), Pytorch 1.13 (Facebook Inc.), and auxiliary libraries of OpenCV 4.8 (Intel Inc.), TorchIO 0.19 (Engineering and Physical Sciences Research Council, EPSRC), Pandas 1.5 (NumFOCUS Inc.), and NumPy 1.24 (NumFOCUS Inc.). The experiments are performed on GeForce RTX 2060 GPU with Cuda 11.0 (NVIDIA Inc.), and Core i5 CPU (Intel Inc.).

For model training, all experiments set the batch size to 64, and the initial learning rate to 1×10^{-4} with a learning rate decay strategy. we use the largest available spine CT image datasets, VerSe2019 and VerSe2020 [32], for experiments and randomly split them into a training set, a validation set, and a test set by 7:1:2. Each model underwent 100 training epochs, culminating in a comprehensive evaluation at the end of the training phase. We introduce five evaluation metrics, including the Dice coefficient, Hausdorff distance, F1 score, average symmetric surface distance (ASSD), and precision, to evaluate the segmentation performance of each model. Additionally, for models that incorporate the spine-aware module, we adopt classification accuracy (namely Aware-ACC) as an evaluation metric to gauge spine-aware performance.

2) Ablation Study: To validate the proposed Spine-aware VNet, we conduct five ablation experiments. The ablation models include the full model, the model without spine-awareness, the model without channel attention, the model without weighted joint loss function, and the baseline model 3D V-Net, as presented in Table I. All ablation experiments are performed on adaptive threshold-based sampling mode. Our Spine-aware VNet ultimately achieves a Dice coefficient of 0.912±0.055, a Hausdorff distance of 6.108±1.994, and an aware-accuracy of 0.937±0.067 on the test set, yielding optimal performance in all evaluation metrics. Compared to the baseline model, our Dice increased by 2.59%, Hausdorff distance decreased by 24.16%, and both standard deviations are smaller, indicating an improvement and stabilization of the segmentation results. This improvement comes from our spine-awareness strategy, the channel attention, and the weighted joint loss function, as evidenced by the following three experiments: (1) Compared to the full model, removing the Spine-awareness decreases Dice by 1.75% and raises Hausdorff distance by 38.74%. The spine-awareness is the core module of our model, which makes the most significant impact on the segmentation performance. Without it, the model has no multi-task learning ability and hence aware accuracy. (2) Removing the channel attention decreases Dice by 1.43%, raises Hausdorff distance by 20.11%, and decreases aware accuracy by 0.96%. Channel attention is applied to the skip connections of the segmentation backbone to balance the negative/synergistic features of the awareness paths to the segmentation paths. Therefore it shows a greater impact on segmentation performance and less impact on aware accuracy. (3) Removing the weighted joint loss decreases Dice by 3.18%, raises Hausdorff distance by 9.14%, and decreases aware accuracy by 0.64%, where the best weights are $W_{\text{aware}} : W_{\text{Seg}} : W_{\text{Comp}} = 2 : 30 : 50$. Due to the simplicity of the awareness task, unweighted loss causes an overwhelming dominance of awareness task and leaves segmentation task

TABLE I
THE ABLATION EXPERIMENT RESULTS OF SPINE-AWARE VNET

Sampling Mode	Comparison Model	Evaluation Metric					
		Dice (std.)	Hausdorff (std.)	F1 (std.)	ASSD (std.)	Precision (std.)	Aware-ACC (std.)
Adaptive Threshold-based Sampling Mode	Spine-aware VNet	0.912 (0.055)	6.108 (1.994)	0.920 (0.050)	0.137 (0.151)	0.917 (0.047)	0.937 (0.067)
	w/o. Spine-awareness	0.896 (0.084)	8.474 (2.768)	0.916 (0.066)	0.175 (0.243)	0.906 (0.065)	– –
	w/o. Channel Attention	0.899 (0.122)	7.336 (3.593)	0.920 (0.065)	0.139 (0.219)	0.915 (0.086)	0.928 (0.069)
	w/o. Weighted Loss	0.883 (0.120)	6.666 (3.318)	0.906 (0.076)	0.188 (0.354)	0.887 (0.100)	0.943 (0.067)
	3D V-Net	0.889 (0.113)	8.054 (2.798)	0.912 (0.068)	0.190 (0.284)	0.891 (0.072)	– –
Uniform Sampling Mode	3D V-Net	0.540 (0.332)	13.446 (8.024)	0.599 (0.311)	1.693 (2.416)	0.829 (0.215)	– –

TABLE II
THE ABLATION EXPERIMENT RESULTS OF DIFFERENT SAMPLING PATCH SIZE

Sampling Patch Size	Comparison Model	Evaluation Metric				
		Dice (std.)	Hausdorff (std.)	F1 (std.)	ASSD (std.)	Precision (std.)
16×16×16	3D V-Net	0.5956 (0.348)	8.448 (5.262)	0.687 (0.305)	1.239 (1.678)	0.877 (0.205)
	Spine-aware VNet	0.854 (0.082)	3.818 (1.016)	0.863 (0.05)	0.186 (0.082)	0.912 (0.057)
32×32×32	3D V-Net	0.889 (0.113)	8.054 (2.798)	0.912 (0.068)	0.19 (0.284)	0.891 (0.072)
	Spine-aware VNet	0.912 (0.055)	6.108 (1.994)	0.92 (0.050)	0.137 (0.151)	0.917 (0.047)
96×96×96	3D V-Net	0.886 (0.138)	14.753 (10.83)	0.94 (0.032)	0.159 (0.109)	0.989 (0.012)
	Spine-aware VNet	0.901 (0.021)	12.625 (2.806)	0.942 (0.017)	0.507 (0.158)	0.958 (0.029)

inadequately trained, which is indicated by the higher Aware-ACC and degraded segmentation performance.

3) Sampling Mode Comparison: To validate the proposed adaptive threshold-based sampling mode, we take 3D V-Net, the most popular model for 3D medical image segmentation, as the baseline model, and conduct comparison experiments for the conventional uniform sampling mode and our adaptive threshold-based sampling mode. To better show the efficiency of our method, only 50 patches of $32 \times 32 \times 32$ samples are set per case, according to the typical volume occupied by a spine in a thoracic-abdominal CT image. The inputs to both modes are raw CT images without any preprocessing. The results are shown in Table I. Under direct input of the raw CT image, the Dice coefficient improves by 64.63% and the Hausdorff distance decreases by 40.10% through our sampling mode.

Our method addresses segmentation under small sampling patches for clinical scenarios with limited computational resources. In this study, ablation experiments with different sampling patch sizes are conducted to compare the segmentation performance of our model and the benchmark model (3D V-Net) under 16×16×16, 32×32×32 and 96×96×96 patch sizes, respectively. As shown in Table II, our model significantly outperforms the benchmark at small patch sizes with an improvement of 43.38% in the dice coefficient. However, this gap gradually narrows as the patch size increases, giving our model an advantage over the benchmark with 2.58% and 1.69% in the dice coefficient at middle and large sizes, respectively. Moreover, the results of standard deviation state that our model provides superior segmentation stability to the baseline regardless of any size. To balance the segmentation accuracy and efficiency, we eventually set patch sizes as 32×32×32.

4) Model Comparison: As an upstream subtask of this study, spine segmentation is fundamental to the final centroid angle calculation. To demonstrate our improvement, we compare our model with six advanced spine segmentation methods: 1) **nnU-Net** [33], which is a famous self-configuring general segmentation model; 2) **RUnT** [34] with a constrain of edge feature fusion by UNet and transformer; 3) **MPVS** [35], which is a two-step approach consisted with a pixel-link convolutional neural network and a multi-label dilated residual network; 4) **3D VNet+Morphology** [36], combining CNN with K-means and K-NN; 5) **Iterative 3D UNet** [37], which segments vertebrae one by one according to the number of

TABLE III
THE COMPARISON RESULTS OF SPINE SEGMENTATION ON CT IMAGE

Reference	Model	Dice
Lessmann et al. [37]	Iterative 3D UNet	0.846
F. Isensee et al. [33]	nnU-Net	0.869
HAO XU et al. [34]	RUnT	0.884
S. Dabiri et al. [35]	MPVS	0.890
Altini, N. et al. [36]	3D VNet+Morphology	0.892
Ours	Spine-aware VNet	0.912

visible vertebrae. The results are shown in Table III. The dice coefficient for our model is 7.801%, 4.948%, 3.167%, 2.47%, and 2.242% higher than [33], [34], [35], [36] and [37], respectively.

B. Vertebrae Recognition in Sagittal Plane

Existing research lacks the annotation data for vertebrae and arch classification in the sagittal plane CT images. To demonstrate the generalization performance of our sagittal plane vertebrae recognition method in various vertebral conditions, 40 standard spine cases and 20 pathological spine cases with typical vertebral lesions from the VerSe dataset are randomly selected. The corresponding sub-datasets, known as the health and pathology datasets, are created accordingly. In particular, it should be noted that the production of the health and pathology sub-datasets is completed with the experiment results invisible, thereby ensuring unbiased results.

For each case in the health dataset, we implement sagittal vertebrae recognition by two individual paths and the compound method, respectively. They correspondingly refer to the output of three stages, vertebrae recognition based on IAC (Method B.2), vertebrae recognition based on CPD (Method B.3), and outlier elimination based on vertebral linkage angle (COMP, Method B.4). Under the guidance and supervision of a clinician, we count the number of vertebrae contained, the total number of regions, the number of recognized vertebrae and the output of the total region at each stage for each image. Then we compute five evaluation metrics, including accuracy, precision, recall, and specificity, to comprehensively show the recognition performance of each stage.

The results of the four evaluation metrics are shown in Table IV. The confusion matrixes are shown in Fig. 8. On the health dataset, our compound method (H-COMP) achieves an accuracy of 0.911±0.085, a precision of 0.937±0.099, a recall of 0.846±0.180, and a specificity of 0.952±0.077. On the pathology dataset, our compound method (P-COMP) achieves an accuracy of 0.819±0.097, a precision of 0.864±0.238, a recall of 0.614±0.222, and a specificity of 0.945±0.077. It reveals a high level of integrative performance of our method for the vertebrae recognition task. As visualized by the box plot (Fig. 9), our compound method outperforms CPD and IAC for both healthy and pathological spines. For example, on the healthy spine, H-IAC and H-CPD reach an accuracy of 0.794±0.130 and 0.840±0.072 respectively, with a mean value of 0.817. After integration and optimization, H-COMP gets an improvement of 14.74% and 8.45% compared to the above two methods respectively, and 11.51% compared to their mean value. On the pathological spine, P-IAC and P-CPD reach an accuracy of 0.709±0.157 and 0.777±0.077 respectively, with a mean value of 0.743. After integration and optimization, P-COMP gets an improvement of 15.52% and 5.41% compared to the above two methods respectively, and 10.23% compared to their mean value. Furthermore, both IAC and CPD show advantages and disadvantages under different evaluation metrics and different spine conditions. As a result, the idea of compounding the two branches is effective and leads to a notable complementarity.

TABLE IV
THE EXPERIMENT RESULTS OF SAGITTAL VERTEBRAE RECOGNITION

Comparison Stage	Evaluation Metric			
	Accuracy (std.)	Precision (std.)	Recall (std.)	Specificity (std.)
H-IAC	0.794 (0.130)	0.736 (0.165)	0.856 (0.186)	0.721 (0.223)
H-CPD	0.840 (0.072)	0.766 (0.092)	0.971 (0.038)	0.719 (0.144)
H-COMP	0.911 (0.085)	0.937 (0.099)	0.846 (0.180)	0.952 (0.077)
P-IAC	0.709 (0.157)	0.663 (0.209)	0.758 (0.216)	0.649 (0.285)
P-CPD	0.777 (0.077)	0.698 (0.117)	0.851 (0.135)	0.713 (0.124)
P-COMP	0.819 (0.097)	0.864 (0.238)	0.614 (0.222)	0.945 (0.077)

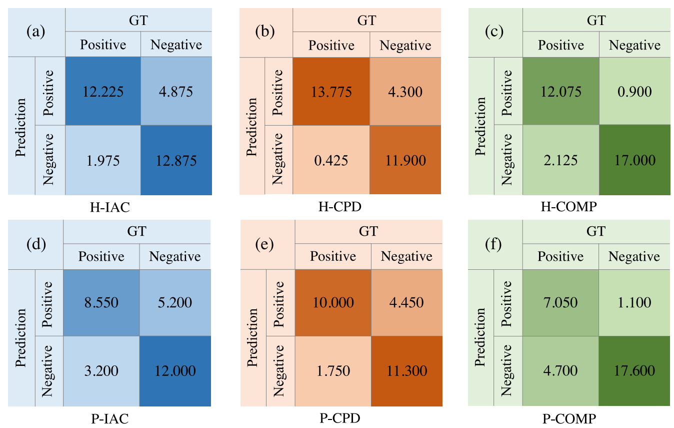

Fig. 8. The confusion matrixes of the vertebrae recognition on the health dataset (a∼c) and pathological dataset (d∼f) by the IAC, CPD, and COMP.

C. Automated Centroid Angle Measurement

To evaluate our automated CA measurements, we compare the automated measurement results from our application with the manual measurement results from an experienced clinician on spine surgeon. This comparison experiment is performed on 30 random preoperative CT images of spinal disease, comprising 108 pairs of adjacent CA measurements and 122 pairs of non-adjacent CA measurements. On each CT image, we first complete accurate manual measurements and use them as ground truths. We then load this CT image in our application

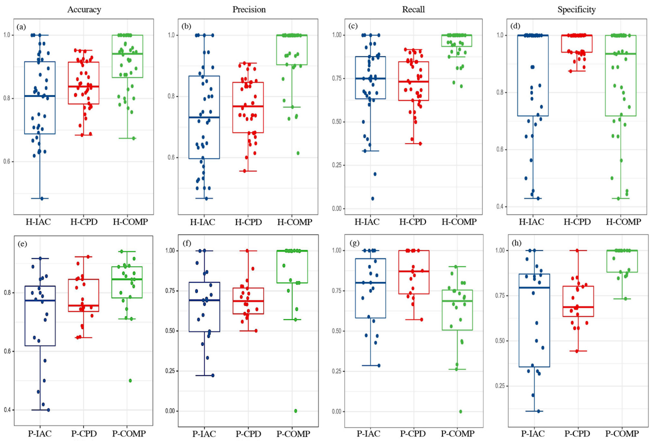

Fig. 9. The box plots of the vertebrae recognition on the health dataset (a~d) and pathological dataset (e~h) by the IAC, CPD, and COMP.

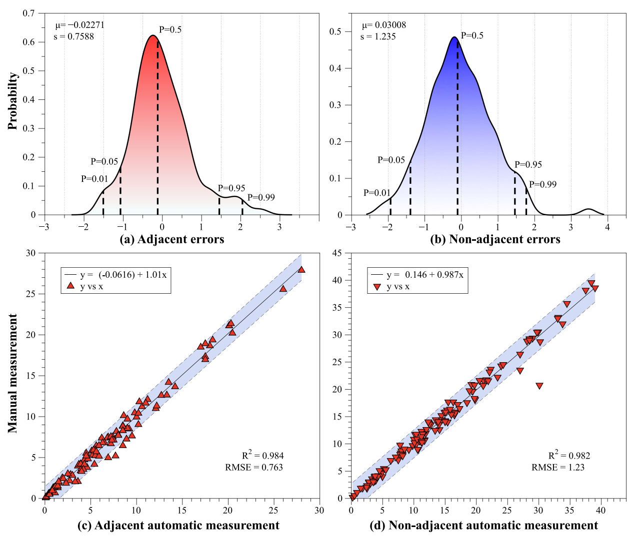

Fig. 10. Error distribution (a~b) and linear fit analysis (b~c) of the adjacent and non-adjacent situation.

and automatically measure CA of the corresponding vertebral sections.

For adjacent cases, compared to manual measurements, the mean absolute error (MAE) of our automated measurements is 0.578 degrees and the mean relative error (MRE) is 8.075% (i.e., 91.925% accuracy). For non-adjacent cases, the MAE of our automated measurements is 0.772 degrees and the MRE is 5.503% (i.e., 94.497% accuracy). The MAE in both situations is 0.681, and the MRE is 6.298%. As shown in Fig. 10(a~b), we draw the error distribution graphs for both situations, which demonstrates that our automated measurement protocol is able to achieve remarkably low errors in an absolute majority of cases. For adjacent vertebrae, the log-normal parameters are $\mu = -0.023$ and $\sigma = 0.759$; For non-adjacent vertebrae, $\mu = -0.030$ and $\sigma = 1.235$. In addition, we analyze the data pairs of automatic and manual measurements by linear fitting. As shown in Fig. 10(c~d), the adjacent cases achieve a slope of $k_1 = 1.010$ and a bias of $b_1 = 0.061$, with $R_1^2 = 0.984$ and $RMSE_1 = 0.763$. The non-adjacent cases achieve a slope of $k_2 = 0.987$ and a bias of $b_2 = 0.146$, with $R_2^2 = 0.982$ and $RMSE_2 = 1.230$. The slopes $k_{1/2} \approx 1$ and biases $b_{1/2} \approx 0$ indicate that our automated measurements provide strong consistency with manual measurements. The scatter plots demonstrate that for both adjacent and non-adjacent vertebrae, relatively small CA correspond to smaller measurement errors, which also account for most of the cases.

IV. Discussion

This study addresses a previously underexplored issue in the field of spinal disease therapy: the preoperative rod design for the robotic-assisted screw-rod system implantation. A series of algorithms are proposed to build a complete preoperative rod design method, accompanied by a corresponding software plugin. In robotic-assisted implantation of screw-rod systems, the rod serves as a vital component, stabilizing the vertebral arch and lamina, particularly in surgeries involving vertebral fractures where rods are essential for fixing and stabilizing the affected spinal section. The alignment of the rod's curvature with the spine is recognized as a critical determinant of postoperative stability. Compared with other spine curvature measurements mostly used for scoliosis assessment, which are impractical for robotic-assisted implantation of screw-rod systems, we enable automated spine curvature measurement from preoperative CT images and apply it to robotic-assisted rod design for the first time. In addition, our Slicer-based plugin can also assist in determining the length, shape, and placement of the rod. This ensures that the rod can perfectly aligned with the patient's spinal curvature, thereby optimizing mechanical properties and improving surgical outcomes.

3D spine segmentation is a fundamental task in both centroidal angle measurement and rod design, where computational efficiency and segmentation accuracy are pivotal for clinical applicability. Compared to 2D segmentation [38], 3D segmentation faces serious memory limitations in clinical settings, which necessitate smaller input sizes for 3D patches. The traditional uniform sampling approach requires a large number of patches to adequately cover the entire spine, complicating the process and leading to inefficiencies. Furthermore, many studies still rely on V-Net [39] that struggle to consistently perceive stable spine features, frequently cause misidentification, and leave "impurities" in segmentation maps, especially in case of small sampling patches and few sampling numbers. Our proposed Spine-aware VNet with a threshold-based sampling mode solves the above sampling and segmentation challenges, achieving a computationally efficient and accurate 3D spine segmentation.

In detail, regarding computational efficiency, a new 3D sampling mode with the adaptive thresholded CT images as probability maps is proposed, leveraging the inherently high CT values of the spinal bones. This sampling mode significantly reduces the patches from hundreds to tens per image for full spine coverage, thereby accelerating calculation speed and lowering equipment requirements. Therefore, our method facilitates spine segmentation in a more clinically friendly manner. Regarding segmentation accuracy, a 3D spine segmentation model featuring multi-scale multi-task learning, namely Spine-aware Vnet is built. Experimental results demonstrate that simultaneous spine awareness benefits the segmentation performance. On one hand, our spine-aware strategy minimizes the "impurities" caused by misidentification, particularly in small $32 \times 32 \times 32$ sampling patches. On the other hand, our segmentation lock mitigates the negative impact of invalid patches, thereby improving training efficiency.

To the best of our knowledge, this research first proposes the task of vertebra recognition in sagittal CT slices, which is an indispensable step in rod design for robotic-assisted screw-rod systems. A compound method of image attribute clustering (IAC) and corner point detection (CPD) is proposed, fulfilling satisfactory recognition accuracy. Furthermore, the vertebral features utilized in this method are consistent with the clinician's intuitive perception, such as the shape properties of the vertebrae, offering strong interpretability.

Ultimately, by integrating the above two steps and CA measurement algorithm, a Slicer-based plugin is developed for the preoperative rod design of robotic-assisted screw-rod systems. For surgeons, this is a highly clinical-friendly application, which accomplishes the rod design from scratch and requires only simple user manipulation and raw CT images without any preprocessing. Especially for novice doctors or country hospitals with poor computing facilities, compared to freehand surgery without preoperative rod design [40], our application can assist them in performing robotic-assisted screw-rod implantation more conveniently and confidently. For patients, our application contributes to the safety of spine surgery by developing a robotic-assisted implantation of screw-rod system that is tailored to the natural curvature of their spine. This personalized approach improves surgical success rates and enhances postoperative rehabilitation outcomes, ultimately advancing patient care in spinal surgery.

Our study meticulously addresses various preoperative pathologies, particularly spinal deformities, through advanced algorithms that optimize rod design. By utilizing sophisticated spine segmentation and vertebrae recognition techniques, we accurately characterize anatomical variations resulting from these pathologies. The incorporation of centroid angle allows personalized rod designs tailored to each patient's unique spinal curvature, accommodating a wide range of anatomical complexities in both pathological and non-pathological conditions. Moreover, distinct rod design templates specific to different spinal pathologies will be continuously developed in the future, since some rare cases may still require additional rod specifications and designs.

However, our method is still facing some limitations. Because our vertebra recognition relies on predefined geometric features, its robustness to special cases where the vertebral structure is damaged, e.g., fractures, remains to be further optimized. Currently, only centroid angles on central sagittal slices are measured, which restricts the direction of implantation from posterior to anterior. However, in practical clinical scenarios, some rare spinal conditions may demand a slight tilting of the screw-rod system toward the coronal plane, especially in cases of severe coronal scoliosis [41], [42]. While the current version of our plugin does not automatically address coronal plane measurement, it allows surgeons to manually alter the rod shape during the adjustment phase if scoliosis is evident in the 3D spine model. This manual flexibility ensures that the rod design better conforms to the patient's anatomical requirements. In the future, we are committed to expanding our plugin to include coronal plane measurements, thus improving our tool's utility and effectiveness in complex surgical scenarios.

Our study builds upon rigorous clinical research [21], [30] and consensus among orthopedic surgeons. Close collaboration with clinical experts ensures the proposed pipeline aligns with current clinical practices. However, a current limitation is the absence of comparative studies against traditional screw-rod system implantation to quantitatively assess improvements in rod quality and reductions in surgical complications. Future research will prioritize conducting these clinical validations, supported by collaborative efforts with surgeons and long-term patient observations.

V. Conclusion

This study achieves centroid angle measurement from CT images for preoperative rod design of robotic-assisted screw-rod systems implantation in an efficient, automatic, accurate, and clinical-friendly manner. We have innovatively proposed and experimentally validated a multi-scale and multi-task 3D spine segmentation method with adaptive sampling, integrated sagittal vertebrae recognition, and automatic centroid angle measurement techniques. Additionally, this research combines the above stages to develop a Slicer-based plugin for the rod design of robotic-assisted screw-rod systems implantation, which is of significant clinical value. Our automatic and efficient preoperative rod design system facilitates the customization of robotic-assisted screw-rod systems, representing a substantial advancement toward personalized spinal disease treatment.

Acknowledgment

The content is solely the responsibility of the authors and does not necessarily represent the official views of the sponsor.

References

[1] M. L. Ferreira et al., "Global, regional, and national burden of low back pain, 1990-2020, its attributable risk factors, and projections to 2050: A systematic analysis of the global burden of disease study 2021," *Lancet Rheumatol.*, vol. 5, no. 6, pp. e316–e329, 2023.

[2] Y. Liu et al., "Spinal cord injury: Global burden from 1990 to 2019 and projections up to 2030 using Bayesian age-period-cohort analysis," *Front. Neurol.*, vol. 14, Dec. 2023, Art. no. 1304153.

[3] J. McAviney, C. Roberts, B. Sullivan, A. J. Alevras, P. L. Graham, and B. T. Brown, "The prevalence of adult de novo scoliosis: A systematic review and meta-analysis," *Eur. Spine J.*, vol. 29, no. 12, pp. 2960–2969, 2020.

[4] T. Driscoll et al., "The global burden of occupationally related low back pain: Estimates from the global burden of disease 2010 study," *Ann. Rheumatic Dis.*, vol. 73, no. 6, pp. 975–981, 2014.

[5] S. Rafi, N. Munshi, A. Abbas, R. H. Shaikh, and I. Hashmi, "Comparative analysis of pedicle screw versus hybrid instrumentation in adolescent idiopathic scoliosis surgery," *J. Neurosci. Rural Pract.*, vol. 7, no. 4, pp. 550–553, 2016.

[6] A. F. Mavrogenis, C. Vottis, G. Triantafyllopoulos, P. J. Papagelopoulos, and S. G. Pneumaticos, "PEEK rod systems for the spine," *Eur. J. Orthopaed. Surgery Traumatol.*, vol. 24, pp. 111–116, Jul. 2014.

[7] Y.-K. Xu, P.-W. Weng, S.-H. Chen, and S.-C. Lin, "Biomechanical comparisons of dynamic fixators with rod-rod and screw-spacer joints on lumbar hybrid fixation," *Clin. Biomech.*, vol. 104, Apr. 2023, Art. no. 105943.

[8] M. D'Souza, J. Gendreau, A. Feng, L. H. Kim, A. L. Ho, and A. Veeravagu, "Robotic-assisted spine surgery: History, efficacy, cost, and future trends," *Robot. Surgery, Res. Rev.*, vol. 6, pp. 9–23, Nov. 2019.

[9] S. C. Overley, S. K. Cho, A. I. Mehta, and P. M. Arnold, "Navigation and robotics in spinal surgery: Where are we now?" *Neurosurgery*, vol. 80, no. 3, pp. S86–S99, 2017.

[10] M. Shoham et al., "Robotic assisted spinal surgery–from concept to clinical practice," *Comput. Aided Surgery*, vol. 12, no. 2, pp. 105–115, 2007.

[11] U. Spetzger, A. V. Schilling, G. Winkler, J. Wahrburg, and A. König, "The past, present and future of minimally invasive spine surgery: A review and speculative outlook," *Minim. Invasive Therapy Allied Technol.*, vol. 22, no. 4, pp. 227–241, 2013.

[12] P. A. Helm, R. Teichman, S. L. Hartmann, and D. Simon, "Spinal navigation and imaging: History, trends, and future," *IEEE Trans. Med. Imag.*, vol. 34, no. 8, pp. 1738–1746, Jan. 2015.

[13] R. Schaffert, J. Wang, P. Fischer, A. Borsdorf, and A. Maier, "Learning an attention model for robust 2-D/3-D registration using point-to-plane correspondences," *IEEE Trans. Med. Imag.*, vol. 39, no. 10, pp. 3159–3174, Oct. 2020.

[14] D. Knez, B. Likar, F. Pernuš, and T. Vrtovec, "Computer-assisted screw size and insertion trajectory planning for pedicle screw placement surgery," *IEEE Trans. Med. Imag.*, vol. 35, no. 6, pp. 1420–1430, Jun. 2016.

[15] A. Y. Moufid, T. Cloche, S. Ghailane, A. Ounajim, T. Vendeuvre, and O. Gille, "Mismatch between rod bending and actual post-operative lordosis in lumbar arthrodesis with poly axial screws," *Orthopaed. Traumatol., Surgery Res.*, vol. 105, no. 6, pp. 1143–1148, 2019.

[16] L. MacLean et al., "Comparison of accuracy, revision, and perioperative outcomes in robot-assisted spine surgeries: Systematic review and meta-analysis," *J. Neurosurg., Spine*, vol. 1, pp. 1–13, Jul. 2024.

[17] X. Wei et al., "Correlations between the sagittal plane parameters of the spine and pelvis and lumbar disc degeneration," *J. Orthopaed. Surgery Res.*, vol. 13, no. 1, pp. 1–9, 2018.

[18] J.-Y. Hong, S.-W. Suh, H. N. Modi, C.-Y. Hur, H.-R. Song, and J.-H. Ryu, "Centroid method: Reliable method to determine the coronal curvature of scoliosis: A case control study comparing with the cobb method," *Spine*, vol. 36, no. 13, pp. E855–E861, 2011.

[19] Y.-L. Chen, "Vertebral centroid measurement of lumbar lordosis compared with the cobb technique," *Spine*, vol. 24, no. 17, p. 1786, 1999.

[20] W. B. Katzman et al., "Reliability of sagittal vertical axis measurement and association with measures of age-related hyperkyphosis," *J. Phys. Therapy Sci.*, vol. 30, no. 12, pp. 1417–1423, 2018.

[21] L. Han et al., "Biomechanical and clinical study of rod curvature in single-segment posterior lumbar interbody fusion," *Front. Bioeng. Biotechnol.*, vol. 10, Mar. 2022, Art. no. 824688.

[22] N. Otsu, "A threshold selection method from gray-level histograms," *IEEE Trans. Syst., Man, Cybern.*, vol. 9, no. 1, pp. 62–66, Jan. 1979.

[23] F. Milletari, N. Navab, and S.-A. Ahmadi, "V-Net: Fully convolutional neural networks for volumetric medical image segmentation," in *Proc. 4th Int. Conf. 3D Vis. (3DV)*, 2016, pp. 565–571.

[24] L.-C. Chen, G. Papandreou, I. Kokkinos, K. Murphy, and A. L. Yuille, "Deeplab: Semantic image segmentation with deep convolutional nets, atrous convolution, and fully connected CRFs," *IEEE Trans. Pattern Anal. Mach. Intell.*, vol. 40, no. 4, pp. 834–848, Apr. 2018.

[25] K. He, X. Zhang, S. Ren, and J. Sun, "Spatial pyramid pooling in deep convolutional networks for visual recognition," *IEEE Trans. Pattern Anal. Mach. Intell.*, vol. 37, no. 9, pp. 1904–1916, Sep. 2015.

[26] L. He, X. Ren, Q. Gao, X. Zhao, B. Yao, and Y. Chao, "The connected-component labeling problem: A review of state-of-the-art algorithms," *Pattern Recognit.*, vol. 70, pp. 25–43, Oct. 2017.

[27] M.-K. Hu, "Visual pattern recognition by moment invariants," *IRE Trans. Inf. theory*, vol. 8, no. 2, pp. 179–187, Feb. 1962.

[28] Z. Xu, X. Baojie, and W. Guoxin, "Canny edge detection based on open CV," in *Proc. 13th IEEE Int. Conf. Electron. Meas. Instrum. (ICEMI)*, 2017, pp. 53–56.

[29] D. H. Douglas and T. K. Peucker, "Algorithms for the reduction of the number of points required to represent a digitized line or its caricature," *Cartographica, Int. J. Geograph. Inf. Geovisual.*, vol. 10, no. 2, pp. 112–122, 1973.

[30] Z. Shi et al., "Use of the sagittal Cobb* angle to guide the rod bending in the treatment of thoracolumbar fractures: A retrospective clinical study," *J. Orthopaed. Surgery Res.*, vol. 15, no. 1, pp. 1–6, 2020.

[31] M. von Atzigen et al., "Reducing residual forces in spinal fusion using a custom-built rod bending machine," *Comput. Methods Programs Biomed.*, vol. 247, Apr. 2024, Art. no. 108096.

[32] A. Sekuboyina et al., "VerSe: A vertebrae labelling and segmentation benchmark for multi-detector CT images," *Med. Image Anal.*, vol. 73, Oct. 2021, Art. no. 102166.

[33] F. Isensee, P. F. Jaeger, S. A. Kohl, J. Petersen, and K. H. Maier-Hein, "nnU-Net: A self-configuring method for deep learning-based biomedical image segmentation," *Nature Methods*, vol. 18, no. 2, pp. 203–211, 2021.

[34] H. Xu, X. Cui, C. Li, Z. Tian, J. Liu, and J. Yang, "RUnT: A network combining residual U-net and transformer for vertebral edge feature fusion constrained spine CT image segmentation," *IEEE Access*, vol. 11, pp. 55692–55705, 2023.

[35] S. Dabiri, D. Ma, K. Popuri, and M. F. Beg, "Multi-view parallel vertebra segmentation and identification on computed tomography (CT) images," *Inform. Med. Unlocked*, vol. 34, Oct. 2022, Art. no. 101091.

[36] N. Altini et al., "Segmentation and identification of vertebrae in CT scans using CNN, k-means clustering and k-NN," *Informatics*, vol. 8, no. 2, p. 40, 2021.

[37] N. Lessmann, B. Van Ginneken, P. A. De Jong, and I. Išgum, "Iterative fully convolutional neural networks for automatic vertebra segmentation and identification," *Med. Image Anal.*, vol. 53, pp. 142–155, Apr. 2019.

[38] J. Zhang, L. Gu, G. Han, and X. Liu, "AttR2U-net: A fully automated model for MRI nasopharyngeal carcinoma segmentation based on spatial attention and residual recurrent convolution," *Front. Oncol.*, vol. 11, p. 5699, Jan. 2022.

[39] L. Zhang et al., "Block level skip connections across cascaded V-net for multi-organ segmentation," *IEEE Trans. Med. Imag.*, vol. 39, no. 9, pp. 2782–2793, Sep. 2020.

[40] L. Yu, X. Chen, A. Margalit, H. Peng, G. Qiu, and W. Qian, "Robot-assisted vs freehand pedicle screw fixation in spine surgery–a systematic review and a meta-analysis of comparative studies," *Int. J. Med. Robot. Compu. Assist. Surgery*, vol. 14, no. 3, 2018, Art. no. e1892.

[41] I. Obeid, P. Berjano, C. Lamartina, D. Chopin, L. Boissière, and A. Bourghli, "Classification of coronal imbalance in adult scoliosis and spine deformity: A treatment-oriented guideline," *Eur. Spine J.*, vol. 28, pp. 94–113, Jan. 2019.

[42] H. Bao, P. Yan, Y. Qiu, Z. Liu, and F. Zhu, "Coronal imbalance in degenerative lumbar scoliosis: Prevalence and influence on surgical decision-making for spinal osteotomy," *Bone Joint J.*, vol. 98, no. 9, pp. 1227–1233, 2016.